Supporting information

High interfacial lithium storage capability of hollow porous Mn_2O_3 nanostructures obtained from carbonate precursors

*Rui Liu, Shiqiang Zhao, Miaomiao Zhang, Fan Feng and Qiang Shen**

(Corresponding E-mail: qshen@sdu.edu.cn)

Experimental:

Preparation of carbonate precursors

$MnCO_3$ cubes were synthesized through a slow ion-exchange reaction of solid-state vaterite with aqueous $MnCl_2$, driven by the solubility product difference between vaterite (i.e., the instable polymorph of anhydrous $CaCO_3$, $K_{sp} \sim 7.8 \times 10^{-4}$) and $MnCO_3$ ($K_{sp} \sim 4.9 \times 10^{-5}$) at room temperature. Firstly, vaterite microspheres were synthesized by quickly pouring a 0.33 M $CaCl_2$ solution (25 mL) into a 0.33 M Na_2CO_3 solution (25 mL), which was agitated using an ultrasonic homogenization at 300 W for 15 s. At a short interval of 45 s, the milky solution was filtrated, washed with deionized water for three times and dried at room temperature for 24 h. Secondly, $MnCl_2 \cdot 4H_2O$ was dissolved in deionized water to obtain $MnCl_2$ aqueous solution (0.1 M, 100 mL). And then, under a vigorous stirring, a 0.25 g of vaterite powders was added into the $MnCl_2$ solution at room temperature, and 6 h later the resulting $MnCO_3$ cubes were collected by filtration, washed with deionized water and dried at room temperature for 24 h.

Preparation of porous Mn_2O_3 boxes

By mixing $KMnO_4$ aqueous solution (0.032 M, 1.8 mL) with the freshly prepared $MnCO_3$ powders (0.2 g) at the Mn^{7+}/Mn^{2+} molar ratio of 1:30, the well-described wet-chemical oxidation reaction proceeded outside the surface of $MnCO_3$ cubes under stirring for 10 min and then the unreacted carbonate cores could be removed by the subsequent excess addition of aqueous HCl (1.2

M). And then, the resulting MnO_2 boxes were obtained after centrifugation, washed for three times with deionized water and dried at 80 ^{o}C for 6 h. Finally, the dried MnO_2 precursors were annealed at 600 ^{o}C under air atmosphere for 4 h, resulting in the final product of porous Mn_2O_3 boxes defined as sample Mn_2O_3-1 in context.

It should be emphasized that, similar to sample Mn_2O_3-1, one comparative Mn_2O_3 product defined as sample Mn_2O_3-2 was prepared at the Mn^{7+}/Mn^{2+} molar ratio of 1:1.5. Furthermore, another comparative Mn_2O_3 was prepared through the direct decomposition of $MnCO_3$ precursor at 600 ^{o}C for 4 h, referred to as sample Mn_2O_3-3.

Material characterization

Powder X-ray diffraction (XRD, Rigaku D/max-2400, Cu-Kα) was used to characterize the phase compositions of precursors and/or products. Scanning electron microscopy (SEM, JEOL, JSM-6700F), transmission electron microscopy (TEM, JEOL, JEM-2100) and high-resolution TEM (HR TEM) were used for the microscopic morphology observations. The thermal analysis of thermogravimetry (TGA) was performed on a SDT Q600 apparatus under air atmosphere, with a heating rate of 10^{o}C/min from room temperature to 800^{o}C. Specific surface area of each Mn_2O_3 sample was measured on a Micromeritics ASAP 2020 sorptometer, and the corresponding pore size distribution was evaluated using Barrett-Joyner-Halenda method.

Electrochemical characterization

After dispersing Mn_2O_3 sample, acetylene black and sodium alginate at a weight ratio of 70:20:10 in deionized water, the resulting homogeneous slurry was pasted onto a pure copper foil and dried at 80 ^{o}C for 12 h. And then, the foil was cut into discs (12 mm in diameter) and used as working electrodes with the mass loading of ~0.9 mg cm^{-2}. CR2032-type coin cells were assembled in an argon-filled glove box using lithium metal as counter electrode, nickel foam as current collector, glass fibers as separator, and 1 M $LiPF_6$ in a mixed solvent of ethylene carbonate (EC), dimethylcarbonate (DMC) and diethyl carbonate (DEC) (1:1:1, v/v/v) as electrolyte. Charge-discharge tests were performed on a Land CT2001A system (Wuhan, Landian) within the potential range of 0.01 - 3 V (*vs.* Li/Li^{+}). Electrochemical impedance spectroscopy (EIS) tests were measured on an electrochemical workstation (Materials Mates 510, Italy) in a frequency range from 100 kHz to 10.0 mHz with AC voltage amplitude of 10 mV at open-circuit voltage.

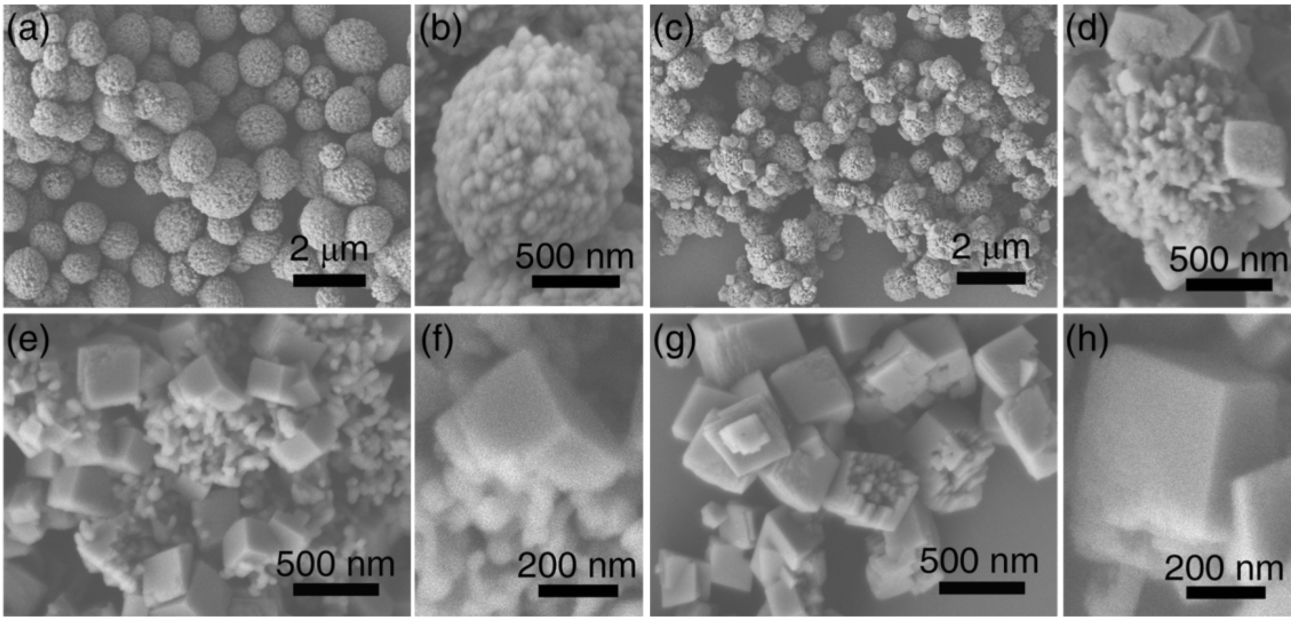

Fig. S1 SEM images of the raw material of crystalline vaterite and its transformed products incubated in aqueous $MnCl_2$ solution at the time intervals of (a, b) 0, (c, d) 2, (e, f) 4 and (g, h) 6 h.

As shown in panels (a) and (b), the raw material of crystalline vaterite was freshly obtained prior to its ion-exchange reaction within $MnCl_2$ aqueous solution, possessing a spherical structure with the diameter of ~1.0 μm. The solubility product of precipitate $MnCO_3$ (4.9×10^{-5}) is lower than that of crystalline vaterite (7.8×10^{-4}) at room temperature, which implies a slow release of Ca^{2+} ions within the medium of aqueous $MnCl_2$ solution and the subsequent precipitation of crystalline $MnCO_3$ outside the surface of each vaterite aggregate.

At the reaction time of 2 h, $MnCO_3$ cubes could be observed outside the surface of spherical vaterite, shown in the panels (c) and (d) of Fig. S1. With the increase of reaction time, the surface of spherical vaterite seemed to be destroyed and covered by cube-shaped $MnCO_3$ with a relatively large average particle size (the panels (e) and (f) of Fig. S1). Finally, at the reaction time of 6 h only the seemingly cube-shaped $MnCO_3$ were obtained, showing a smooth surface for each cube mostly (the panels (g) and (h) of Fig. S1).

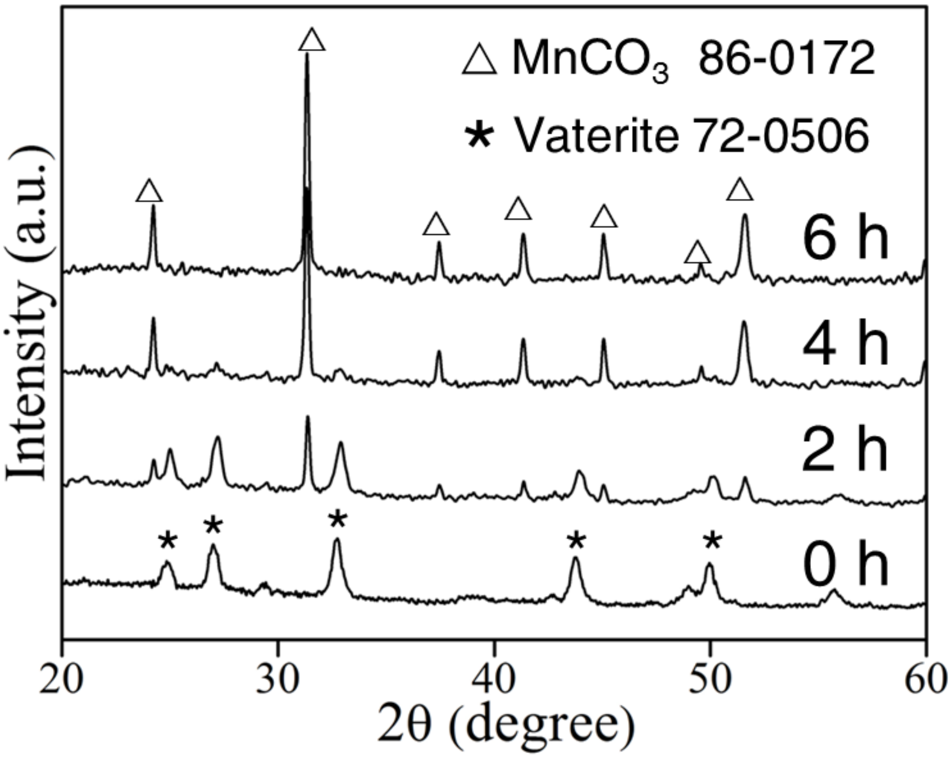

Fig. S2 XRD patterns of the raw material of crystalline vaterite and its transformed products incubated in aqueous $MnCl_2$ solution at the time intervals of 0, 2, 4 and 6 h.

The combination of time-dependent SEM pictures and corresponding XRD results proves the gradual transformation of spherical $CaCO_3$ to $MnCO_3$ cubes, indicates that this procedure adopted for the preparation of Mn_2O_3 can be defined as the experimental method of carbonate precursors as shown in Fig. 1a.

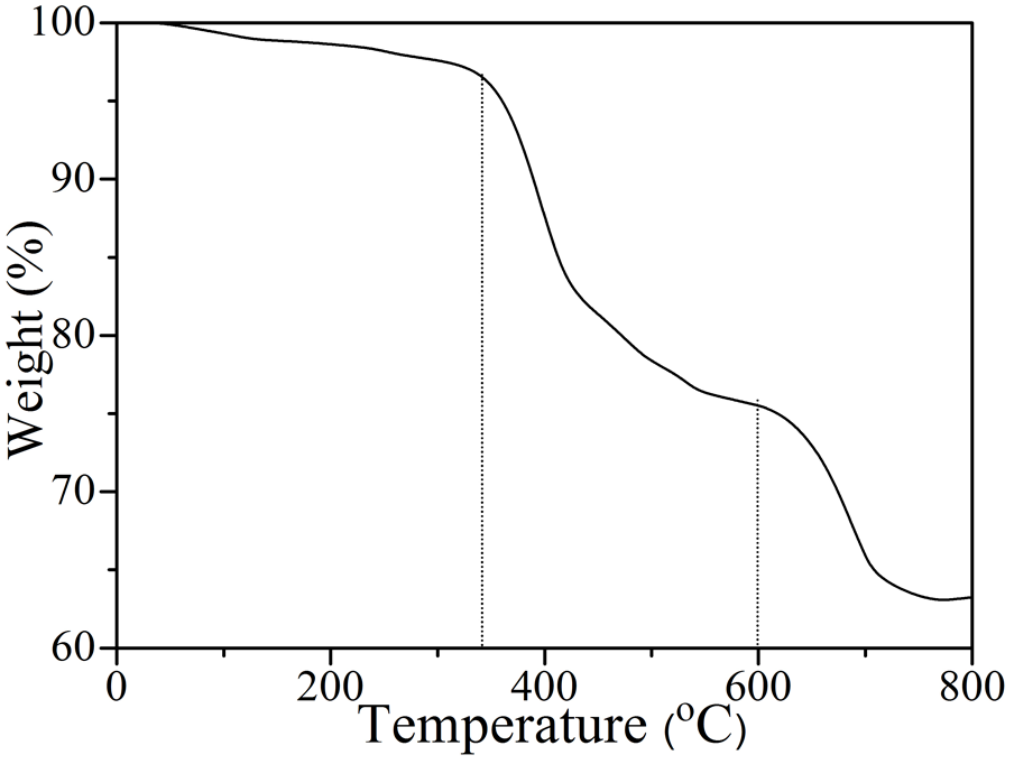

Fig. S3 TGA curve of precursor $MnCO_3$ recorded at a heating rate of 10°C/min from room temperature to 800 °C.

Under air atmosphere, the thermal decomposition of $MnCO_3$ may result in the valance-different manganese oxides of MnO_2, Mn_2O_3, Mn_3O_4 and MnO, depending upon the sintering temperature. Herein, a calcination temperature of 600 °C is selected according to the TGA results shown as below.

As shown in Fig. S3, the first steep weight loss beginning at ~340 °C is associated with the transformation of $MnCO_3$ to MnO_2, while the second steep weight loss starting at ~600 °C relates to the transformation of MnO_2 to Mn_2O_3.

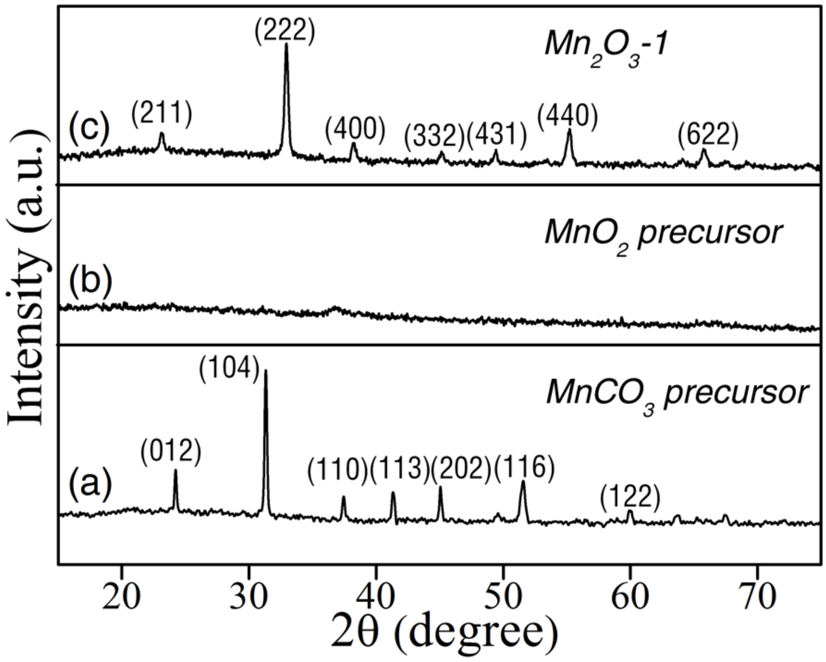

Fig. S4 XRD patterns of (a) $MnCO_3$ cubes, (b) MnO_2 boxes and (c) porous Mn_2O_3 boxes.

After the ion-exchange reaction of aqueous Mn^{2+} and solid-state $CaCO_3$, the resulting $MnCO_3$ crystallites are faint yellow in color, defined as the initial carbonate precursor. As shown in Fig. S4a, XRD pattern of the $MnCO_3$ can be indexed using the standard data of rhombohedral structure (JCPDS No. 44-1472).

After the $KMnO_4$-assisted wet-chemical oxidation of solid-state $MnCO_3$, the resulting in MnO_2 is brown in color and possesses an amorphous nature (Fig. S4b).

After the 4-h annealing of amorphous MnO_2 at 600 °C, the final product is black in color and its XRD diffraction pattern coincides well with that of cubic Mn_2O_3 (JCPDS No. 41-1442) as shown in Fig. S4c.

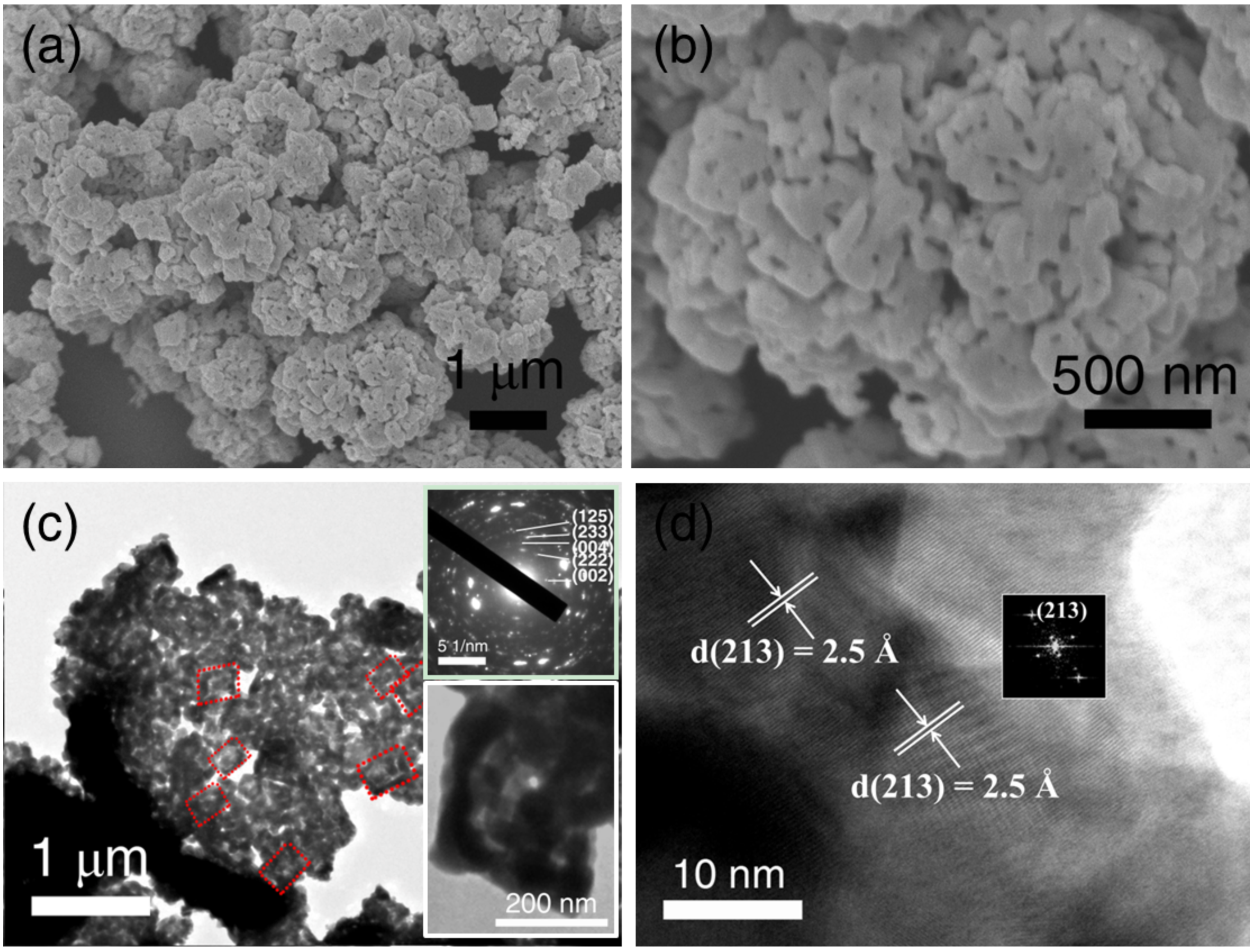

Fig. S5 (a, b) SEM, (c) TEM and (d) HRTEM images of hollow porous Mn_2O_3-2 nanostructures. In panel (c), an inset in the bottom right corner is the magnified TEM picture of a porous box and the inset in the upper right corner is the ED pattern of powdered Mn_2O_3-2. In panel (d), the lattice fringes of crystal plane (213) with an interplanar spacing of 0.25 nm are marked along with an inserted Fourier-transformed (FFT) pattern.

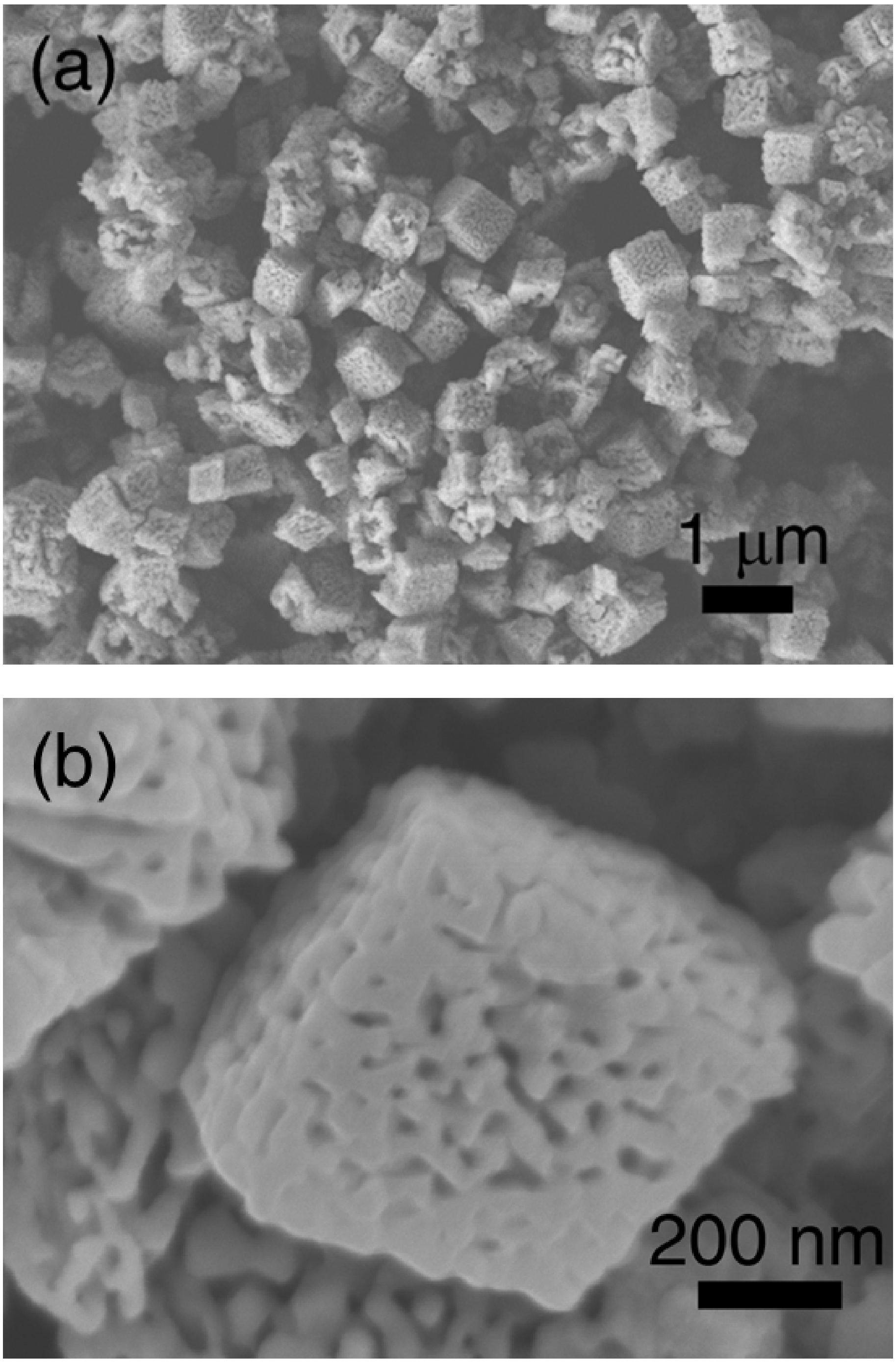

Fig. S6 SEM images of porous Mn_2O_3-3 cubes obtained from the direct calcination of precursor $MnCO_3$ at 600 ^oC for 4 h: (a), overall view; (b), close-up view.

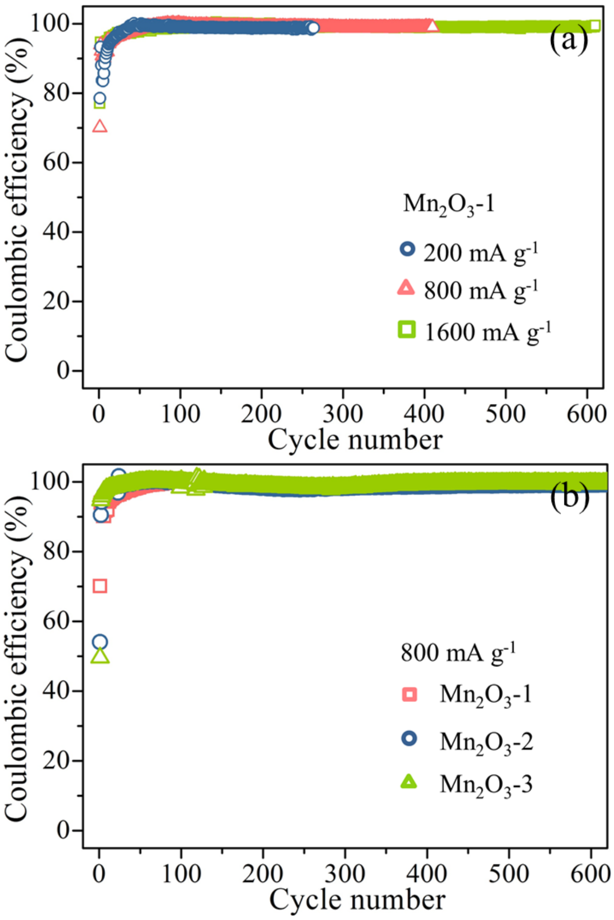

Fig. S7 Coulombic efficiencies (CEs) of various electrodes: (a), Mn_2O_3-1 recorded at different current rates; (b) different anodes operated at 800 mA g^{-1}.

As shown in panel (a), at the current densities of 200, 800 and 1600 mA g^{-1}, sample Mn_2O_3-1 shows the low CEs of 78%, 70% and 77%, respectively, which can be attributed to the formation of solid electrolyte interface (SEI) films and/or electrolyte degradation. Over the 20th charge-discharge cycle at 200, 800 and 1600 mA g^{-1}, the obtained CEs are 96.4%, 96.2% and 96.6%, respectively. In the 80th charge-discharge cycle and thereafter, the exhibiting CEs reach a constant of ~99.3% at each current rate. These indicate that, for the high surface area of porous Mn_2O_3 boxes obtained from carbonate precursors, the high current rate facilitates the reversibility of the electrode reaction especially after the 80th charge-discharge cycle.

As shown in panel (b), at the current density of 800 mA g^{-1}, samples Mn_2O_3-1, Mn_2O_3-2 and Mn_2O_3-3 interestingly show the different initial Coulombic efficiencies of 70%, 54% and 50%, respectively, which may be simply assigned to their different specific surface areas of 52.23 (Mn_2O_3-1), 17.63 (Mn_2O_3-2) and 9.23 m^2 g^{-1} (Mn_2O_3-3) as shown in Fig. 4a-c.

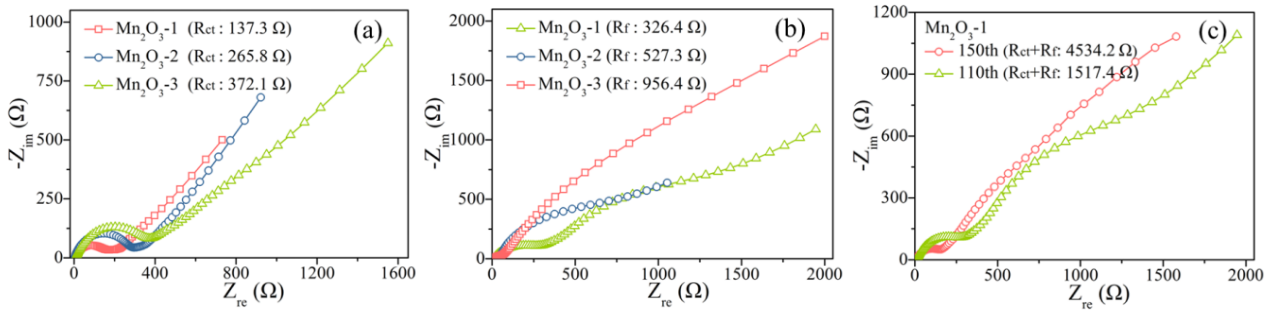

Fig. S8 EIS results of various electrodes operated at different conditions: (a), at open-circuit voltage; (b, c), after the 110th and 150th cycles at 1600 mA g^{-1}, respectively.

The high frequency region of the single semicircle (panel (a)) or a depressed semicircle in the high frequency region (panel (b) or (c)) is indicative of surface-film resistance R_f at the electrode-electrolyte interface, while another semicircle in the middle frequency region (panel (b) or (c)) or the middle frequency region of the single semicircle (panel (a)) corresponds to charge-transfer resistance R_{ct}. For a comparison purpose, an equivalent circuit has been applied to fit these EIS data.

From panel (a), it can be observed that all the samples have a similar Nyquist plot in curve shape, composed of one semicircle at the high and middle frequency region and a line at the low frequency region. The charge-transfer resistance of Mn_2O_3-1 is 137.3 Ω, lower than the 265.8 Ω of Mn_2O_3-2 and 372.1 Ω of Mn_2O_3-3, which means the higher specific surface area and the lower charge-transfer resistance.

Generally, a passive layer called the solid-electrolyte interphase (SEI) should form during the first discharge process, which is also determined by the surface properties of Mn_2O_3. From panel (b), In the 110th cycle at 1600 mA g^{-1}, the R_f value of Mn_2O_3-1(326.4 Ω) is smaller than those of Mn_2O_3-2 (527.3 Ω) and Mn_2O_3-3 (956.4 Ω), which means the higher surface area and the lower surface-film resistance.

From panel (c), the R_{ct} + R_f value of Mn_2O_3-1 in the 110th cycle is 1517.4 Ω, while that of Mn_2O_3-1 in the 150th cycle is 4534.2 Ω. Considering a constant Li-ion diffusion within bulk active substance determined by its inherent characteristics, the smaller value of R_{ct} + R_f and the higher the charge transfer ability of the exactly "same" working electrode. By comparison, these suggest that the total value of reversible capacity (i.e., not the interfacial storage) should decrease from the 110th to 150th cycle; however, as shown in Fig. 3c the reversible capacity of porous Mn_2O_3-1 boxes starts to keep increasing after 80 cycles. Therefore, an extra non-faradaic contribution may gradually emerge to compensate the general capacity fade occurring after the 80 charge-discharge cycles.

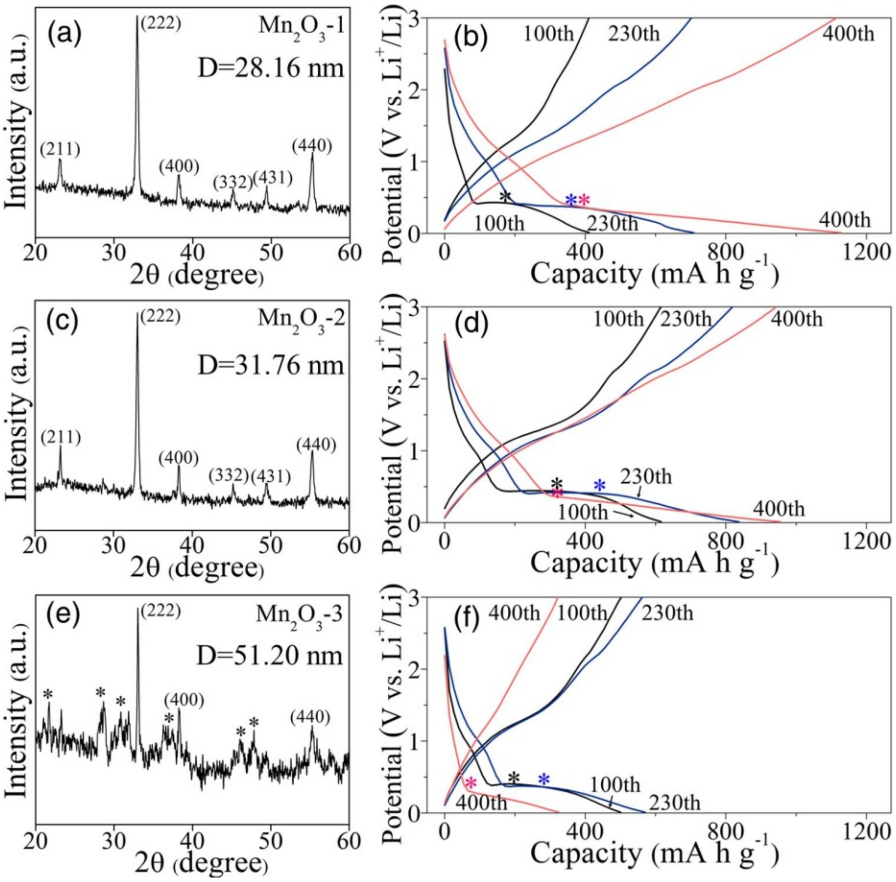

Fig. S9 (left) XRD patterns and (right) representative voltage profiles of (a, b) Mn_2O_3-1, (c, d) Mn_2O_3-2 and (e, f) Mn_2O_3-3.

As shown in these XRD patterns, diffraction peaks can be indexed using the standard data of cubic Mn_2O_3 (JCPDS No.: 41-1442) and D represents the average particle size of Mn_2O_3 calculated using Scherrer equation and the reflection of (222) crystal plane. In panel (e), XRD reflections marked by asterisk indicate the coexistence of impurity assigned to $Ca_2Mn_3O_8$ (JCPDS No.: 73-2290), suggesting that, after the ion-exchange reaction of aqueous Mn^{2+} and solid-state $CaCO_3$, the residual $CaCO_3$ may be completely encapsulated with the interior of $MnCO_3$ cubes.

In each voltage profile asterisk symbol is indicative of the beginning of the corresponding interfacial Li storage contribution, determined shortly after the end of voltage plateau. At 800 mA g^{-1} the discharge capacities of Mn_2O_3-1 are 411, 709 and 1127 mA h g^{-1} with the interfacial storage parts of 237, 362 and 718 mA h g^{-1} in the 100th, 230th and 400th cycles, respectively (Fig. S7b). Similarly, at 800 mA g^{-1} the 100th, 230th and 400th reversible capacities / the interfacial storage contributions of Mn_2O_3-2 electrode are 616/249, 837/380 and 955/643 mA h g^{-1}, while those of Mn_2O_3-3 electrode are 501/307, 570/336 and 322/211 mA h g^{-1}.

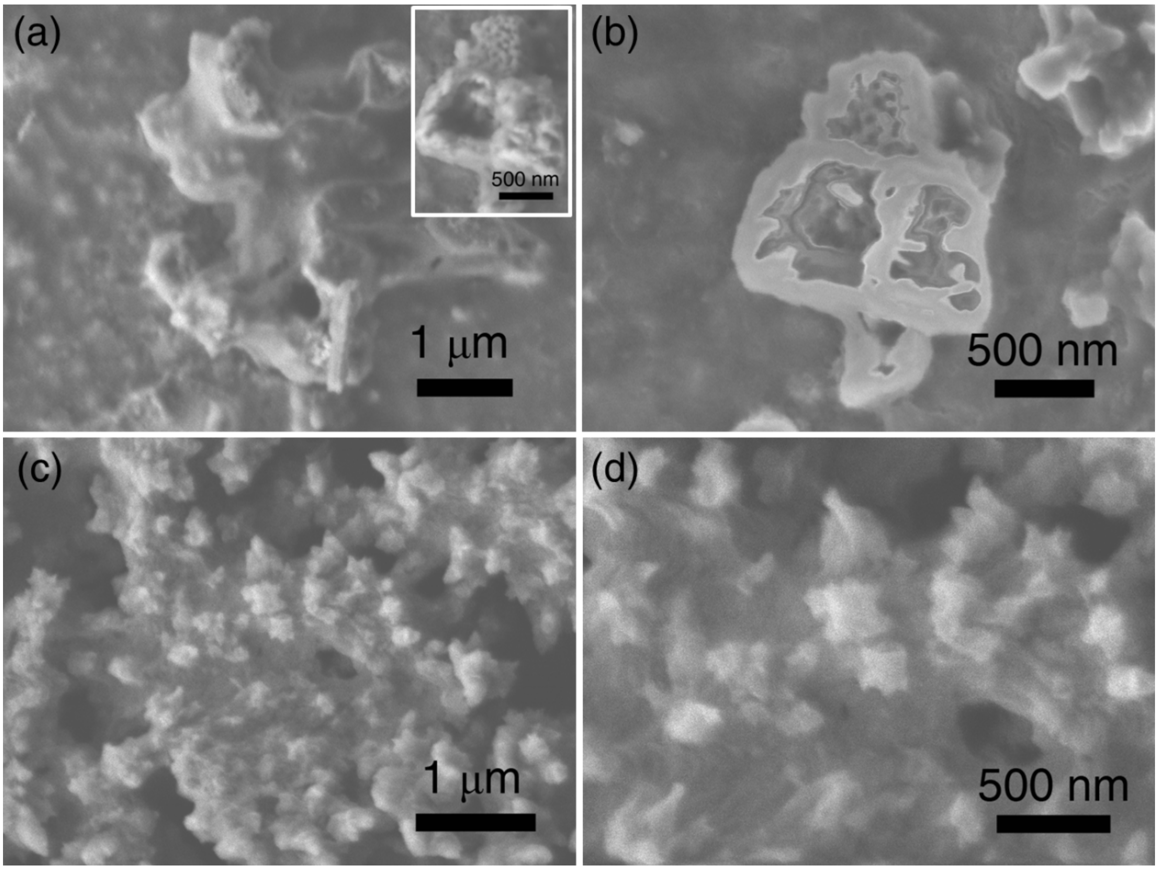

Fig. S10 SEM images of active substances taken after the 110th cycle at 1600 mA g^{-1}: (a, b), hollow porous Mn_2O_3-1 boxes; (c, d) porous Mn_2O_3-3 cubes.

After 110 cycles at 1600 mA g^{-1}, the porous Mn_2O_3 boxes still maintain the hollow porous structures (panels (a) and (b)), while the porous Mn_2O_3 cubes are totally pulverized under these electrochemical conditions (panels (c) and (d)). By estimation, the shell thickness of electrochemically cycled Mn_2O_3-1 boxes is around 85 nm (panel (b)), which is bigger than that of as-prepared porous Mn_2O_3-1 as shown in Fig. 1d. This may be due to the formation of SEI layer outsides the particles' surface and confirms the structural stability during the continuous charge-discharge processes. Moreover, the possibly layered arrangement of adjacent shells at nanoscale could further answer for the emerging interfacial non-faradic capacity therein.